

LA-UR-15-20089 (Accepted Manuscript)

## Nonlinear electric field structures in the inner magnetosphere

Malaspina, D.M.  
Andersson, L.  
Ergun, R. E.  
Wygant, J. R.  
Bonnell, J. W.  
Kletzing, C.  
Reeves, Geoffrey D.  
Skoug, Ruth M.  
Larsen, Brian Arthur

Provided by the author(s) and the Los Alamos National Laboratory (2016-09-27).

**To be published in:** Geophysical Research Letters

**DOI to publisher's version:** 10.1002/2014GL061109

**Permalink to record:** <http://permalink.lanl.gov/object/view?what=info:lanl-repo/lareport/LA-UR-15-20089>

**Disclaimer:**

Approved for public release. Los Alamos National Laboratory, an affirmative action/equal opportunity employer, is operated by the Los Alamos National Security, LLC for the National Nuclear Security Administration of the U.S. Department of Energy under contract DE-AC52-06NA25396. Los Alamos National Laboratory strongly supports academic freedom and a researcher's right to publish; as an institution, however, the Laboratory does not endorse the viewpoint of a publication or guarantee its technical correctness.

# **Electric Field Structures and Waves at Plasma Boundaries in the Inner Magnetosphere**

David M. Malaspina

Laboratory for Atmospheric and Space Physics, University of Colorado,  
Boulder, Colorado, USA

John R. Wygant

School of Physics and Astronomy, University of Minnesota, Minneapolis,  
MN, USA

Robert E. Ergun

Laboratory for Atmospheric and Space Physics, University of Colorado,  
Boulder, Colorado, USA  
Department of Astrophysical and Planetary Sciences, University of Colorado,  
Boulder, Colorado, USA

Geoff D. Reeves

Los Alamos National Laboratory, Los Alamos, New Mexico, 87544, USA

Ruth M. Skoug

Los Alamos National Laboratory, Los Alamos, New Mexico, 87544, USA

Brian A. Larsen

Los Alamos National Laboratory, Los Alamos, New Mexico, 87544, USA

---

David M. Malaspina, Laboratory for Atmospheric and Space Physics, University of Colorado, Boulder, Colorado 80303, USA. (David.Malaspina@colorado.edu)

John Wygant, School of Physics and Astronomy, University of Minnesota, Minneapolis, MN 55455, USA (wygan001@umn.edu)

Robert E. Ergun, Laboratory for Atmospheric and Space Physics, University of Colorado, Boulder, Colorado, 80303, USA. (ree@lasp.colorado.edu)

Geoff D. Reeves, Los Alamos National Laboratory Los Alamos, New Mexico, 87544, USA (reeves@lanl.gov)

Ruth M. Skoug, Los Alamos National Laboratory Los Alamos, New Mexico, 87544, USA (rskoug@lanl.gov)

Brian A. Larsen, Los Alamos National Laboratory Los Alamos, New Mexico, 87544, USA (balarsen@lanl.gov)

**Abstract.**

Recent observations by the Van Allen Probes spacecraft have demonstrated that a variety of electric field structures and nonlinear waves frequently occur in the inner terrestrial magnetosphere, including phase space holes, kinetic field-line resonances, nonlinear whistler-mode waves, and several types of double layer. However, it is unclear whether such structures and waves have a significant impact on the dynamics of the inner magnetosphere, including the radiation belts and ring current. To make progress toward quantifying their importance, this study statistically evaluates the correlation of such structures and waves with plasma boundaries. A strong correlation is found. These statistical results, combined with observations of electric field activity at propagating plasma boundaries, are consistent with the identification of these boundaries as the source of free energy responsible for generating the electric field structures and nonlinear waves of interest. Therefore, the ability of these structures and waves to influence plasma in the inner magnetosphere is governed by the spatial extent and dynamics of macroscopic plasma boundaries in that region.

## 1. Introduction

Recent observations by the Van Allen Probes have demonstrated that a wide variety of electric field structures and nonlinear waves regularly occur in the terrestrial inner magnetosphere. Such structures and waves include electron double layers [Mozer *et al.*, 2013], nonlinear whistler-mode waves [Mozer *et al.*, 2014], kinetic-scale field line resonances [Chaston *et al.*, 2014], electron phase space holes [Malaspina *et al.*, 2014], relativistic electron double layers [Malaspina *et al.*, 2014], and strong double layers [Malaspina *et al.*, 2014]. These structures and waves are readily identified in high-cadence burst waveform data [Mozer *et al.*, 2013] or in spectral wave data as broadband wave power [Malaspina *et al.*, 2014].

It has been shown that some of these structures and waves interact strongly with electrons and ions, in some cases leading to prompt acceleration [Mozer *et al.*, 2013, 2014; Artemyev *et al.*, 2014]. Further, such structures and waves are commonly observed at radial distances associated with the radiation belts and ring current [Malaspina *et al.*, 2014]. With such properties, these structures and waves may constitute an element of inner magnetospheric wave dynamics that current models do not consider.

Is the inclusion of such structures and waves important for modeling inner magnetospheric dynamics? The answer can only be determined by quantifying the impact that these structures and waves have on the plasma in the inner magnetosphere. Toward that end, this study addresses two specific questions: (1) how strongly are these waves and structures correlated with plasma boundaries? (2) Does the region of wave and structure generation travel with propagating plasma boundaries in the inner magnetosphere?

The first question is motivated by *Chaston et al.* [2014] and *Malaspina et al.* [2014] who reported qualitatively that many instances of high amplitude electric field structures and nonlinear waves in the inner magnetosphere appear to coincide with plasma boundaries. Further, observations of electron double layers [*Mozzer et al.*, 2013] and nonlinear whistler-mode waves [*Mozzer et al.*, 2014] were also found to coincide with plasma boundaries. If the occurrence of the structures and waves listed above is strongly correlated with plasma boundaries, then the macro-scale dynamics of these boundaries, including their spatial extent and propagation dynamics through the inner magnetosphere, may strongly modulate the efficiency of wave-particle interactions involving the described structures and waves.

The second question is designed to test whether the described electric field structures and nonlinear waves are being continually generated at plasma boundaries. If plasma boundaries continually generate these structures and waves, and these structures and waves deposit their energy efficiently into the plasma through wave-particle interactions, then observations of these structures and waves represent localized regions where the energy associated with macro-scale motions of plasma and magnetic fields is actively being dissipated at micro-scales. Knowledge of the locations and mechanisms by which macro-scale flow energy is dissipated is important for understanding a range of dynamic process in the inner magnetosphere, including the slowing of earthward flow bursts [*Miyashita et al.*, 2012].

In this work, plasma boundaries are defined using abrupt transitions in particle flux, such as those that occur at dispersionless injection fronts (e.g. *Birn et al.* [1997] and references therein) or at the Earthward edge of the plasma sheet (e.g. *Cao et al.* [2011]

and references therein). A detailed discussion of plasma boundary definitions appears in Section 3.

The remainder of this paper is organized as follows. First, relevant instrumentation on the Van Allen Probes and THEMIS spacecraft is described. Then, examples are presented of plasma boundaries identified in the inner magnetosphere. A statistical study of such plasma boundaries and their relation to electric field structures and nonlinear wave activity is then used to address question (1). Plasma boundary propagation delays between spacecraft are then used to address question (2). A discussion of the results is presented, followed by conclusions.

## 2. Instrumentation

The Van Allen Probes are twin spinning spacecraft orbiting the Earth in approximately geotransfer orbits ( $\sim 350$  km x  $\sim 6.6 R_E$ ). They complete a full rotation every  $\sim 11$  seconds and a full orbit about Earth every  $\sim 9$  hours. The two spacecraft have slightly different orbits, such that inter-spacecraft separation becomes small ( $< 2 R_E$ ) for  $\sim 8$  days every  $\sim 72$  days. The Van Allen Probes complete a full orbital precession through all local times approximately every two years.

This study uses data from several instruments on the Van Allen Probes. Spacecraft potential, electric and magnetic field data are provided by the EFW [Wygant *et al.*, 2013] and EMFISIS [Kletzing *et al.*, 2013] instruments. Electron and ion data are provided by the HOPE ( $< 50$  keV) [Funsten *et al.*, 2013], MagEIS ( $\sim 30$  keV to  $\sim 1$  MeV) [Blake *et al.*, 2013], and REPT ( $\sim 1$  MeV -  $\sim 20$  MeV) [Baker *et al.*, 2013] instruments. In their standard operating modes, HOPE, MagEIS, and REPT data (post-calibration) includes

flux as a function of energy for electrons once every  $\sim 22$ s,  $\sim 10$ s, and  $\sim 10$ s, respectively.

We do not examine pitch angle information in this work.

EFW and EMFISIS sample voltages from four spheres in the spacecraft spin plane ( $V_1$ ,  $V_2$ ,  $V_3$ ,  $V_4$ ), each at the end of 50m wire booms, and two spheres along the spacecraft spin axis ( $V_5$ ,  $V_6$ ) at the end of 7m rigid booms. The spacecraft spin axis is oriented  $\sim 15$  degrees from the spacecraft-Sun line. Spheres are sampled both as single-ended voltage measurements ( $V_1$  through  $V_6$  referenced to the spacecraft body potential) and as dipole electric field measurements (e.g.  $E_{12} = (V_1 - V_2)/L$ , for effective probe separation  $L$ ). EFW and EMFISIS also record magnetic field measurements made by a three-axis search coil magnetometer (SCM) and EMFISIS samples a three-axis fluxgate magnetometer (FGM) at speeds up to 64 samples per second. A variety of data products at a range of cadences are produced from these measurements. See *Wygant et al.* [2013] and *Kletzing et al.* [2013] for details. This work primarily uses power spectra produced on-board by EFW. These power spectra cover frequencies below 8192 Hz. Spectra are calculated every 1/8 of a second, then time-averaged over 1 second and reported every 4 seconds.

Portions of this study use data from the THEMIS spacecraft, specifically the EFI electric field instrument [*Bonnell et al.*; *Cully et al.*, 2008], FGM fluxgate magnetometer [*Auster et al.*, 2008], as well as the ESA ( $< 30$ keV) [*McFadden et al.*, 2008] and SST ( $\sim 30$ keV to  $\sim 800$  keV) [*Angelopoulos*, 2008] particle instruments. Further details on the THEMIS spacecraft and their orbits can be found in *Angelopoulos* [2008].

### 3. Plasma Boundaries

Before presenting the results of the statistical study of wave activity near plasma boundaries, the definition of a plasma boundary is discussed and observations exemplifying

each type of boundary identified by this study are shown. In this work, plasma boundaries are defined using electron energy flux derived from HOPE measurements integrated over all pitch angles. Electron energy flux is examined for HOPE 5 keV, 10 keV, 15 keV, 20 keV, and 30 keV energy channels. A plasma boundary is defined as an instance when electron energy flux increases by at a factor of 5 or more during a three-minute window in three or more of these energy channels. The search window slides point by point through each sample of HOPE electron data. A dead-time of 3.5 minutes is imposed after each identified boundary to avoid double counting. All data below McIlwain L shell of 3 are excluded because no naturally occurring sharp plasma boundaries in 10's of keV electrons are observed inside the plasmasphere.

Because spacecraft charging effects complicate measurement of the cold core proton distribution temperature and because accurate plasma boundary propagation velocity measurement are infrequent, the time window over which a change in electron energy flux is used to identify a boundary is empirically defined and not based on a physical scale such as a thermal proton gyroradius. To demonstrate that the obtained results are robust to this empirical boundary definition, statistical results in section 4 are also presented in using steeper (electron energy flux increase by a factor of 5 or more over two minutes in at least three energy channels) and shallower (electron energy flux increase by a factor of 5 or more over four minutes in at least three energy channels) definitions for plasma boundaries.

It is also understood from prior work on dispersionless injections [*Birn et al.*, 1997] that, due to species-specific drifts, an injection front that appears dispersionless in either electrons or ions may not appear dispersionless in the other species, depending on where

the spacecraft crosses the front. In spite of this, plasma boundaries are defined here using only electron energy flux because many of the waves and electrostatic structures of concern to this work are associated with electron, rather than ion, instabilities (e.g. whistler-mode waves and electron double layers).

Figure 1 shows data from one orbit of Van Allen Probe B on 23 June 2013 exhibiting a plasma boundary identified using the above definition. Figures 1a, 1b, and 1c show electron energy flux as a function of electron energy and time from the REPT, MagEIS, and HOPE instruments respectively. Figures 1d, 1e, and 1f display 1 second cadence magnetic field data measured by EMFISIS/FGM. Figure 1d shows the elevation angle of the magnetic field out of the Z GSM plane  $\theta_{Bz} = \tan^{-1} (B_z / \sqrt{B_x^2 + B_y^2})$ . An abrupt increase in  $\theta_{Bz}$  indicates a dipolarization of the ambient magnetic field. 1e shows azimuthal deflection of the magnetic field in the XY GSM plane ( $\phi_{Bxy} = \tan^{-1} (B_y / B_x)$ ). With this definition,  $\phi_{Bxy} = 0$  indicates a magnetic field vector pointing directly tail-ward of Earth. 1f shows  $\phi_{Bxy}$  with a 3-minute running average of the data in 1e removed. 1g shows the negative of the spacecraft potential, calculated as the average of the potentials on the  $V_1$  and  $V_2$  probes. Variation in this quantity near 16:00 and 20:30 UTC indicates sharp changes in plasma density (see for example, *Pedersen et al.* [2008]) associated with crossings of the plasmopause. The abrupt decrease in spacecraft potential near 17:45 UTC is due to spacecraft surface charging by secondary electrons generated by the high flux of  $\sim 10$  keV electrons (e.g. [Whipple, 1981]). 1h shows electric field power spectra, calculated on-board by EFW, measured by the  $E_{12}$  dipole. The color scale has been artificially saturated at  $3.2 (mV/m)^2/Hz$  to emphasize detail in the plot. The solid white line indicates half the electron gyrofrequency ( $0.5f_{ce}$ ). 1i shows EFW magnetic field power

spectra, calculated on-board, where the wave power in all three search coil axes has been summed. The color scale has been again artificially saturated, at  $0.001 \text{ nT}^2/\text{Hz}$ , to bring out detail in the plot.

The event of interest, a near-simultaneous increase in electron energy flux across a range of energies, occurs near 17:45 UTC. The identified plasma boundary is indicated by a vertical dashed line in 1d. The boundary is accompanied by a dipolarization (1d), an azimuthal deflection of the magnetic field (1e), ultra low frequency (ULF) waves in the Pi2 frequency range ( $\sim 11 \text{ mHz}$ ) (1f), sudden onset of broadband electric and magnetic field wave power understood to be signatures of electric field structures and nonlinear waves [Chaston *et al.*, 2014; Malaspina *et al.*, 2014] (1h, 1i), and sudden onset of whistler-mode wave power (1h, 1i). The spacecraft was at low magnetic latitude ( $\sim 4 \text{ deg}$ ), high L-shell ( $\sim 6$ ), and in pre-midnight magnetic local time ( $\sim 21 \text{ MLT}$ ) during the event.

The dipolarization, combined with a sudden onset of whistler-mode wave power near  $0.5f_{ce}$  is consistent with electrons adiabatically energized perpendicular to  $\mathbf{B}$  and therefore unstable whistler-mode wave growth [Smith *et al.*, 1996]. Further, electrons  $> 300 \text{ keV}$  change little during the event, suggesting that the spacecraft never exits the magnetic field region that defines closed drift paths for those particles. Further, the event occurred near the geomagnetic equator, where the spacecraft is less likely to directly encounter the plasma sheet in the inner magnetosphere [Mauk and Meng, 1983; Cao *et al.*, 2011]. Given these properties, this event is most likely a dispersionless injection. Dispersionless injections inside of geosynchronous orbit are not uncommon [Reeves *et al.*, 1996; Nosé *et al.*, 2010], though they are infrequently reported in the literature [Nosé *et al.*, 2010].

Figures 2-4 are presented in the same format as Figure 1, except that spacecraft potential data is not included for Figure 4, as strong spacecraft charging during that time period makes the data interpretation unclear.

Figure 2 shows data from 10 June 2013 on Van Allen Probe A. The boundaries identified in 2 are accompanied by dipolarizations (2d), changes in  $\phi_{Bxy}$  (2e),  $\phi_{Bxy}$  ULF oscillations in the Pi2 range (2f), and decreases of the spacecraft potential consistent with enhanced secondary electron production (2g). Strong, nearly electrostatic broadband wave activity is evident at and near these boundaries (2h, 2i). Kinetic Alfvén wave field line resonances have been identified near 06:00 UTC by analysis of burst data recorded during this interval [Chaston *et al.*, 2014]. A brief interval of weak chorus wave activity occurs after the large dipolarization near 06:00 UTC (2h,22), but the observed chorus frequencies are significantly below the local value of  $0.5f_{ce}$ , implying that the spacecraft is distant from the chorus wave source region [Chum *et al.*, 2003].

The spacecraft exits the plasmopause near 02:10 UTC and re-enters around 07:15 UTC, where the plasmopause location is inferred from spacecraft potential variation (2g) and the appearance of plasmaspheric hiss between 100 Hz and 1 kHz (2i). Between 02:45 and 06:00 UTC, electron energy flux  $\geq 100keV$  is largely absent (with brief returns), despite being abundant before 02:45 and after 06:00 UTC (2a, 2b). Proton energy flux  $\geq 100keV$  is also absent over the same intervals (not shown). This implies that the spacecraft has moved onto field lines that do not support closed drift paths for energies  $\geq 100keV$ . The remaining electron (and proton) energy flux is consistent with that typically observed in the near-Earth plasma sheet [Tang *et al.*, 2009].

Based on these properties, the boundaries in Figure 2 are interpreted as the spacecraft crossing into and out of the horns [*Suszcynsky et al.*, 1993] of the plasmashet at off-equatorial latitudes ( $\sim 20$  deg MLaT). These crossings are likely due to a combination of spacecraft motion and plasma sheet dynamics. Horn crossings are common in Van Allen Probes data, especially between May and August of 2013, when the tilt of Earth's magnetic dipole combined with the orbit of the Van Allen Probes resulted in frequent excursions to magnetic latitudes  $\geq 15$  degrees.

Figure 3 shows data from 30 March 2013 on Van Allen Probe B. The boundary identified in Figure 3 is associated with the plasmopause, evident in 3g as a sharp change in spacecraft potential. The plasmasphere is locally eroded to L-shell  $\approx 3.8$  at this time. Plasmaspheric hiss is evident inside the plasmasphere near 05:00 UTC, while chorus-band waves are observed outside the plasmasphere, after 05:24 UTC (3h, 3i). ULF wave power is evident at the plasmopause in 3d, 3e, and 3f. Broadband wave power is also present at the plasmopause (3h, 3i). The sharp boundary in 10's of keV electrons here is likely due to removal of these electrons inside the plasmasphere due to interaction with plasmaspheric hiss [*Meredith et al.*, 2007]. Sharp 10 keV electron boundaries associated with the plasmopause are relatively rare in the first two years of the Van Allen Probes data compared to events like the one in Figure 1. They only appear in conjunction with a strongly eroded plasmasphere.

Figure 4 shows data from 11 November 2012 on Van Allen Probe B. The boundaries in Figure 4 are distinguished by dropouts of electron flux across a broad range of energies (4a, 4b, 4c). Proton flux also drops out across nearly all energies at the same times (not plotted), indicating the spacecraft is no longer on magnetic field lines representing closed

drift paths for the energies observed to drop out. During the dropouts  $\phi_{Bxy}$  varies strongly (4e). As each dropout ends,  $\theta_{Bz}$  increases sharply (4d). Strong broadband and whistler-mode wave activity is evident throughout this interval (4g, 4h). The highest amplitude broadband waves occur near the flux dropouts.

The properties of this event are consistent with the Van Allen Probes exiting the inner magnetosphere and entering the lobe of the magnetosphere. While rare in the data compared to events similar to Figure 1, events similar to Figure 4 tend to occur during strong geomagnetic activity when the spacecraft are in the dawn sector at geomagnetic latitudes away from the equator.

#### 4. Statistics

All boundaries identified by the algorithm described in Section 3 can be classified into one of the four types presented in that section. For purposes of this study, the physical cause of each identified plasma boundary is unimportant (except in the case of the plasmopause, as discussed below). The focus is instead on the correlation between such boundaries and the electric field structures and nonlinear waves listed in the introduction. Two questions are posed to quantify that correlation: (1) What fraction of plasma boundaries in the inner magnetosphere show broadband wave activity nearby? (2) What fraction of broadband wave activity occurs near plasma boundaries in the inner magnetosphere?

Broadband wave activity is quantified, following [Malaspina et al., 2014], as the sum of the EFW on-board power spectral density of the  $E_{12}$  signal below 100 Hz. While broadband wave power can often exceed 100 Hz (e.g. Figure 2), this limit is imposed to ensure that all whistler-mode waves are excluded. Only spectral bins that are sufficiently

electrostatic ( $E_{12}^2 > 0.1c^2B^2$ ) are retained for consideration, where  $c$  is the speed of light. This criteria excludes nearly all plasmaspheric hiss. The electrostatic criteria used here is looser than that defined in *Malaspina et al.* [2014] ( $E_{12}^2 > c^2B^2$ ), in order to include more kinetic Alfvén wave power [Chaston et al., 2014] while still excluding most hiss power. Spectral bins with high magnetic compressibility are also removed to exclude magnetosonic wave power. High compressibility is defined as when magnetic wave power along the background magnetic field is  $\geq 0.65$  of the total magnetic wave power. Additionally, spectral data are not considered during thruster firings, EFW bias sweeps [Wygant et al., 2013], when HOPE data is unavailable, or when the electric field instrument preamplifiers saturate [Wygant et al., 2013].

All spectral survey data from two years of the Van Allen Probes mission (01 November, 2012–01 November 2014) on both spacecraft are examined. The two year time period was chosen to ensure that the Van Allen Probe completed full orbital precession through all local times.

To answer question (1), all plasma boundaries were identified in this data set using the definition given in Section 3. In all, 357 boundaries were found. Figure 5 shows the magnetic local time and L-shell distribution of the identified boundaries. Twenty-four of these are plasmopause crossings, classified as such because the plasma density, as determined by the upper hybrid resonance line, abruptly transitions across  $50 \text{ cm}^{-3}$  within 30 minutes of the identified boundary. Plasmopause-related boundaries are indicated by red symbols in Figure 5.

None of the plasmopause boundaries show broadband wave activity  $> 2 \text{ mV/m}$  within 30 minutes of the boundary crossing. Because of this, plasmopause boundaries are excluded

from the remainder of the analysis. Qualitatively, broadband electric fields are evident in the wave power spectra near many plasmopause crossings where the plasmasphere is strongly eroded. Yet the broadband wave activity near the plasmopause extends to lower peak frequencies than at other boundaries (Figure 3h, compared to Figure 2h), suggesting that short time-duration electrostatic structures such as double layers and phase space holes are uncommon or of comparatively low amplitude near the plasmopause. Analysis of high rate burst data is required to verify this directly. The broadband wave power that does appear is of much lower amplitude than at other plasma boundaries in the inner magnetosphere. These observations suggest that a property of the plasmopause (likely the associated high density) inhibits the generation of the electric field structures and nonlinear waves responsible for the broadband wave power, as compared to other boundaries such as injection fronts or the inner edge of the plasma sheet. For the remainder of this work, boundary and boundary crossing refer to non-plasmopause boundaries unless explicitly stated.

To quantify the probability of observing broadband wave activity near a boundary, an epoch analysis is performed on the broadband wave amplitudes  $\pm 60$  minutes from the boundaries. Figure 6a shows a series of probability distributions for broadband wave amplitude as a function of distance from the 333 (non-plasmopause) boundary crossings. Probability distributions are normalized to 1 separately for each amplitude bin. Figure 6b shows the number of boundary crossings with broadband wave power amplitude in the range of each amplitude bin. The vertical blue line indicates 333. These data show that all crossings had broadband waves  $\leq 1$  mV/m within 60 minutes. Observation of progressively higher amplitude broadband waves was increasingly rare.

Figure 6a shows that the probability of observing broadband waves with amplitude  $\geq 2$  mV/m is centered on the boundary crossing. Below 2 mV/m, observation probability depends weakly on observation time relative to the boundary. Above  $\geq 2$  mV/m, higher amplitude broadband waves are more likely to be co-located with a plasma boundary and lower amplitude waves are more likely to be observed at or after a boundary crossing.

Table 1 shows the fraction of boundaries with broadband waves of amplitudes  $\geq 2$  mV/m within various times from the boundary crossings. Similar statistics are included for steeper and shallower definitions of a plasma boundary (Section 3) to demonstrate the robustness of this result. In all cases, the correlation is strong between these plasma boundaries the broadband waves indicative of nonlinear waves and kinetic-scale electric field structures. Sharper boundaries are more likely to have broadband waves observed nearby.

To more thoroughly address this correlation, the reverse analysis is also performed. All instances of  $\geq 1$  mV/m broadband wave activity during the studied two-year interval were identified, then the closest plasma boundary (from the list of non-plasmapause boundaries already generated) was identified.

There were 16,460 instances of broadband wave activity  $\geq 2$  mV/m identified (33,559  $\geq 1$  mV/m), where every on-board EFW spectra in the two-year studied time period was examined, excluding times with thruster events, probe saturation, missing HOPE data, and EFW bias sweeps. Figure 7 shows the distribution of broadband wave activity instances in magnetic local time and L-shell. The distribution is qualitatively similar to that found for plasma boundaries.

Epoch analysis was again performed, this time examining the probability of finding a boundary some time away from a given instance of broadband wave activity. Figure 8a shows the resulting probability distributions for times  $\pm 1$  hour from all broadband wave instances. Probability distributions are normalized to 1 for each amplitude bin. Plasma boundaries are most likely to be found coincident with broadband wave activity, and higher wave amplitudes are more tightly co-located with plasma boundaries. At lower broadband amplitudes, the distribution is skewed toward boundaries preceding wave activity. Figure 8b shows the number of broadband wave instances included in each amplitude bin of the plot. Table 2 shows the percentage of  $> 2\text{mV/m}$  broadband wave instances with plasma boundaries nearby. Percentages are also presented for steeper and shallower boundary definitions.

These results, combined with those in Figure 6 and Table 1, demonstrate that  $\sim 90\%$  of plasma boundaries in the inner magnetosphere have  $> 2\text{ mV/m}$  broadband waves within  $\pm 1\text{ hr}$  and that  $\sim 90\%$  of the  $> 2\text{ mV/m}$  broadband wave activity instances in the inner magnetosphere have a plasma boundary within  $\pm 1\text{ hr}$ . Given the relative rarity of the identified plasma boundaries ( $< 400$  over two years), these data demonstrate a strong correlation between plasma boundaries in the inner magnetosphere and the broadband wave power indicative of electric field structures and nonlinear waves.

## 5. Boundary Propagation

Multi-spacecraft observations of plasma boundaries can be used to address whether such plasma boundaries can be the source of free energy for nonlinear wave and electric field structure activity in the inner magnetosphere. Two case studies are presented where it is demonstrated that the onset of broadband wave activity propagates through the

inner magnetosphere at the same rate as other features of the plasma boundary, including magnetic field perturbations and increased electron fluxes. One case study examines an injection front, while the other treats an event more consistent with a crossing out of the so-called plasma sheet horns.

Figure 9 shows a dispersionless injection event as observed by both THEMIS-D ( 9a- 9d) and Van Allen Probe B ( 9e- 9h) on 02 October 2013. 9a and 9b show electron energy flux as a function of energy and time, measured by the SST and ESA instruments, respectively. The energy range plotted in 9a has been expanded beyond the range of the SST instrument to match the range of energies measured by the Van Allen Probes MagEIS instrument. The electron energy flux shown in 9b, near 1 keV and after 05:00 UTC, has saturated the ESA detector. 9c shows the  $B_z$  GSM component of the background magnetic field at THEMIS. 9d shows seven bins of band-pass electric field data from the filter bank data product [Cully, 2007]. The frequency range has been expanded to encompass the full range of frequencies measured by both spacecraft. 9e and 9f show electron energy flux on Van Allen Probe B from the MagEIS and HOPE instruments, respectively. 9g shows  $B_z$  GSM measured by Van Allen Probe B. 9h shows power spectra of the electric field measured by  $E_{12}$  on Van Allen Probe B. Figure 10b shows the relative positions of THEMIS-D and the Van Allen Probes during the time period plotted in Figure 9.

Three independent indicators are used to identify the injection front.  $B_z$ , electron energy flux in the  $\sim 20$  keV energy channel, and broadband electric field amplitude, are each examined for the time of maximum increase within a 15-sample sliding window. The THEMIS and Van Allen Probe FGM data used is sampled at 0.3 Hz and 1 Hz respectively. The THEMIS/ESA and Van Allen Probe HOPE data are sampled at 0.3 Hz and  $\sim 0.045$

Hz. The broadband electric field amplitude is determined from by integrating the band  
pass data and power spectra  $< 100\text{Hz}$ , sampled at  $0.3\text{ Hz}$  and  $0.25\text{ Hz}$ , respectively.  
Figure 10b shows the time associated with the maximum increase of each of the three  
front indicators, for both spacecraft. Error bars represent a  $\pm 1$  sample period uncertainty  
in the location of the front for each quantity.

All three measures yield similar estimates for the time of injection front passage at  
THEMIS-D. At Van Allen Probe B, the three measures give front passage times that  
overlap to within single-sample errors. Table 3 shows the propagation time delay of the  
injection front as it passes from THEMIS-D to Van Allen Probe B as determined by each  
of the three front indicators. Also listed are the associated spacecraft separations in X  
GSM and the derived velocity. L-shell separation is not used here because the geomagnetic  
field is locally disturbed and the spacecraft are closely spaced ( $LT0.5R_E$ ), rendering L  
parameter estimates unreliable. The average X GSM propagation velocity from these  
three measures is then  $42\text{ km/s}$ , consistent with previous observations of injection front  
velocities inside of geosynchronous orbit [Reeves *et al.*, 1996]. These data demonstrate  
that the onset of broadband wave activity propagates with nearly same velocity as the  
injection front.

Figure 11 shows another plasma boundary crossing by multiple spacecraft. 11a and 11e  
show MagEIS electron energy flux on Van Allen Probe A and B, respectively. 11b and  
11f show HOPE electron energy flux. 11c and 11g show  $B_z$ . Finally, 11d and 11h show  
power spectra of the wave electric field. In this example, on 10 June 2013, the boundary  
is more consistent with a crossing out of the plasma sheet horns, due to motion of both

the plasma sheet boundary and the spacecraft. Arguments for this interpretation appear in Section 3.

Figure 12a shows the positions of the two Van Allen Probe spacecraft, as well as GOES-13, which was in the vicinity of the Van Allen Probes during this event. Figure 12b shows the plasma boundary crossing times for this event as determined using the same three indicators in the same manner as in Figure ?? . In this case, the time of broadband wave activity onset precedes the plasma boundary, as determined by  $B_z$  and electron energy flux. Yet the propagation time delays, as determined by all three indicators, match to within single-sample timing errors ( $206.1 \pm 1.4$ s for  $B_z$  data,  $209.4 \pm 31.1$ s for electron energy flux data, and  $212.2 \pm 5.7$ s for electric field data). The close timing correspondence indicates that the region of broadband wave onset is propagating at the same rate as the boundary itself.

## 6. Discussion

The data presented here show a strong correlation between broadband wave power and plasma boundaries in the inner magnetosphere. Data was also presented demonstrating that the region of broadband wave power onset travels with propagating plasma boundaries. These data contain clues as to the mechanisms that generate the electric field structures and nonlinear waves at plasma boundaries. First, in Figures 1h and 2h, it is evident that broadband wave activity can persist on the order of 30 minutes after the crossing of a plasma boundary. The probability distributions in Figures 6 and 8 show that this behavior (wave activity following a boundary crossing) is common. Consider one of the Van Allen Probes observing an injection front. If the front is observed near apogee, the spacecraft altitude changes minimally over 30 minutes. If a rapidly decelerating

injection front ( $\sim 0.011 \text{ km/s}^2$  [*McPherron et al.*, 2011]) traveling Earthward at  $\sim 25 \text{ km/s}$  [*Reeves et al.*, 1996] crosses the spacecraft near apogee ( $6.6 R_E$ ), that front will be tens of thousands of electron gyro radii (several hundred ion gyro radii) away from the spacecraft after 30 minutes, assuming a 250 nT field at the point of boundary crossing and a 10 keV electron or proton. It is therefore unlikely that a feature spatially localized to the front such as a temperature gradient is directly responsible for the electric field structures and waves that persist after a boundary crossing.

Further, broadband wave activity at the plasmopause in Figure 3 is not co-located with the  $> 100 \text{ eV}$  electron plasma boundary. The broadband wave activity is co-located instead with the ULF waves ( $< 0.5 Hz$ ) in 3d, 3e, and 3f. This observation also argues against wave growth directly from a property of the  $> 100 \text{ eV}$  electron boundary.

The data are instead more consistent with Alfvénic waves as the driver for many of the observed electric field structures and waves. It is proposed that large-scale low-frequency Alfvénic fluctuations lead to kinetic Alfvén waves and/or kinetic-scale field line resonances [*Chaston et al.*, 2014]. The localized electric fields associated with the kinetic Alfvén waves [*Hasegawa*, 1976] or kinetic-scale field line resonances may then locally accelerate electrons, leading to double layers and electron phase space holes through streaming instabilities. This process has recently been proposed to explain the abundance of double layers and phase space holes observed in the bursty bulk flow breaking region of the magnetotail [*Stawarz et al.*, 2014; *Ergun et al.*, 2014]. Evidence has been presented previously for large-scale Alfvén waves generating kinetic Alfvén waves, which in turn drive electron beams in the plasma sheet boundary layer [*Wygant et al.*, 2002]. At the near-equatorial magnetic latitudes of the inner magnetosphere sampled by the Van Allen Probes, the

source large-scale Alfvénic fluctuations may be related to the macroscopic motion of the inner edge of the plasma sheet, the Earthward motion of injection fronts [Kepko and Kivelson, 1999], or surface waves at the plasmopause [Daly and Hughes, 1985].

In support of this interpretation, figures 1 through 4 all show a qualitative correspondence between the presence of enhanced  $< 0.5\text{Hz}$  wave power in  $\mathbf{B}$  and broadband wave activity. In particular, broadband activity with a stronger magnetic component, indicative of the kinetic-scale field line resonances described by Chaston *et al.* [2014], is closely associated with enhanced  $< 0.5\text{Hz}$   $\mathbf{B}$  wave power. The more electrostatic enhancements in broadband wave power, indicative of double layers and phase space holes, occur after the peaks in the  $< 0.5\text{Hz}$   $\mathbf{B}$  wave amplitudes (e.g. Figure 2f, 2h, and 2i).

The nonlinear whistler-mode waves reported by Mozer *et al.* [2014] may arise instead from phase trapping of electrons [Kellogg *et al.*, 2010; Mozer *et al.*, 2014] by high amplitude whistler-mode waves. In that case, the association of nonlinear whistler mode waves with plasma boundaries likely exists because the source of free energy for generation of the (initially linear) whistler-mode waves is the magnetic compression associated with Earthward-propagating injection fronts.

## 7. Conclusions

The goal of this study was to address the importance of electric field structures and waves, including double layers, phase space holes, nonlinear whistler-mode waves, and kinetic field line resonances, to inner magnetosphere dynamics. Two specific questions were posed: (1) how strongly are these structures and waves correlated with plasma boundaries? (2) Are plasma boundaries the source of free energy for electric field structure and nonlinear wave activity in the inner magnetosphere?

In answer to (1), it is found that plasma boundaries are strongly correlated with the appearance of these structures and waves, such that  $\sim 92\%$  of identified plasma boundaries show significant electric field structure and wave activity ( $> 2$  mV/m) within  $\pm 1$  hr and  $\sim 91\%$  of electric field structure and wave activity instances ( $> 2$  mV/m) have a plasma boundary within  $\pm 1$  hr. The plasmopause was found to be unique among inner magnetospheric plasma boundaries in that the electric field structures and waves observed were of low amplitude and likely do not include double layers or phase space holes. Two case studies presented in Section 5 demonstrate that the region of electric field structure and wave activity onset propagates with plasma boundaries. This suggests that electric field structures and nonlinear waves are continually generated at the plasma boundary, because electric field structures (e.g. electron phase space holes and double layers) and nonlinear whistler-mode waves have group velocities along magnetic field lines [Mozer *et al.*, 2013, 2014; Malaspina *et al.*, 2014] that are much faster than the effective propagation speeds of plasma boundaries [Reeves *et al.*, 1996]. Therefore, plasma boundaries are likely to be the free energy source for nonlinear wave activity in the inner magnetosphere.

Given these results, we conclude that the ability of the electric field structures and nonlinear waves described in the introduction to influence plasma in the inner magnetosphere through wave-particle interactions, including in the radiation belts and ring current regions, is constrained by the spatial extent and dynamics of macroscopic plasma boundaries in these regions.

**Acknowledgments.** The authors thank the Van Allen Probes team, especially the EFW, EMFISIS, and HOPE teams for their support. This work was funded by NASA

award NAS5-01072. All data used in this work is available from the EFW, EMFISIS, and  
HOPE teams.

## References

- Angelopoulos, V. (2008), The THEMIS Mission, *Space Science Reviews*, *141*, 5–34, doi:  
10.1007/s11214-008-9336-1.
- Artemyev, A. V., O. V. Agapitov, F. Mozer, and V. Krasnoselskikh (2014), Thermal  
electron acceleration by localized bursts of electric field in the radiation belts, *Geophys.*  
*Res. Lett.*, , *41*, 5734–5739, doi:10.1002/2014GL061248.
- Auster, H. U., et al. (2008), The THEMIS Fluxgate Magnetometer, *Space Science Reviews*,  
*141*, 235–264, doi:10.1007/s11214-008-9365-9.
- Baker, D. N., et al. (2013), The Relativistic Electron-Proton Telescope (REPT)  
Instrument on Board the Radiation Belt Storm Probes (RBSP) Spacecraft:  
Characterization of Earth’s Radiation Belt High-Energy Particle Populations, *Space*  
*Science Reviews*, *179*, 337–381, doi:10.1007/s11214-012-9950-9.
- Birn, J., M. F. Thomsen, J. E. Borovsky, G. D. Reeves, D. J. McComas, and R. D. Belian  
(1997), Characteristic plasma properties during dispersionless substorm injections at  
geosynchronous orbit, *J. Geophys. Res.*, , *102*, 2309–2324, doi:10.1029/96JA02870.
- Blake, J. B., et al. (2013), The Magnetic Electron Ion Spectrometer (MagEIS) Instruments  
Aboard the Radiation Belt Storm Probes (RBSP) Spacecraft, *Space Science Reviews*,  
*179*, 383–421, doi:10.1007/s11214-013-9991-8.
- Bonnell, J. W., F. S. Mozer, G. T. Delory, A. J. Hull, R. E. Ergun, C. M. Cully,  
V. Angelopoulos, and P. R. Harvey (), The Electric Field Instrument (EFI) for THEMIS,

*Space Science Reviews.*

Cao, J. B., W. Z. Ding, H. Reme, I. Dandouras, M. Dunlop, Z. X. Liu, and J. Y.

Yang (2011), The statistical studies of the inner boundary of plasma sheet, *Annales*

*Geophysicae*, *29*, 289–298, doi:10.5194/angeo-29-289-2011.

Chaston, C. C., et al. (2014), Observations of kinetic scale field line resonances, *Geophys.*

*Res. Lett.*, *41*, 209–215, doi:10.1002/2013GL058507.

Chum, J., F. Jiříček, J. Smilauer, and D. Shklyar (2003), Magion 5 observations of chorus-

like emissions and their propagation features as inferred from ray-tracing simulation,

*Annales Geophysicae*, *21*, 2293–2302, doi:10.5194/angeo-21-2293-2003.

Cully, C. M. (2007), Electric fields and current sheet structure in magnetospheric plasmas,

Ph.D. thesis, University of Colorado at Boulder.

Cully, C. M., R. E. Ergun, K. Stevens, A. Nammari, and J. Westfall (2008), The THEMIS

Digital Fields Board, *Space Science Reviews*, *141*, 343–355, doi:10.1007/s11214-008-

9417-1.

Daly, R. A., and W. J. Hughes (1985), The effect of hydromagnetic waves on

the shape of the plasmopause boundary, *J. Geophys. Res.*, *90*, 537–542, doi:

10.1029/JA090iA01p00537.

Ergun, R. E., K. A. Goodrich, J. E. Stawarz, L. Andersson, and V. Angelopoulos (2014),

Large-Amplitude Electric Fields Associated with Bursty Bulk Flow Braking in the

Earth’s Plasma Sheet, *Journal of Geophysical Research (Space Physics)*.

Funsten, H. O., et al. (2013), Helium, Oxygen, Proton, and Electron (HOPE) Mass

Spectrometer for the Radiation Belt Storm Probes Mission, *Space Science Reviews*,

*179*, 423–484, doi:10.1007/s11214-013-9968-7.

Hasegawa, A. (1976), Particle acceleration by MHD surface wave and formation of aurora,  
*J. Geophys. Res.*, , *81*, 5083–5090, doi:10.1029/JA081i028p05083.

Kellogg, P. J., C. A. Cattell, K. Goetz, S. J. Monson, and L. B. Wilson, III (2010), Electron trapping and charge transport by large amplitude whistlers, *Geophysical Research Letters*, *37*, L20106, doi:10.1029/2010GL044845.

Kepko, L., and M. Kivelson (1999), Generation of Pi2 pulsations by bursty bulk flows, *J. Geophys. Res.*, , *104*, 25,021–25,034, doi:10.1029/1999JA900361.

Kletzing, C. A., et al. (2013), The Electric and Magnetic Field Instrument Suite and Integrated Science (EMFISIS) on RBSP, *Space Science Reviews*, *179*, 127–181, doi:10.1007/s11214-013-9993-6.

Malaspina, D. M., L. Andersson, R. E. Ergun, J. R. Wygant, J. W. Bonnell, C. Kletzing, G. D. Reeves, R. M. Skoug, and B. A. Larsen (2014), Nonlinear electric field structures in the inner magnetosphere, *Geophys. Res. Lett.*, , *41*, 5693–5701, doi:10.1002/2014GL061109.

Mauk, B. H., and C. I. Meng (1983), Dynamical injections as the source of near geostationary quiet time particle spatial boundaries, *J. Geophys. Res.*, , *88*, 10,011–10,024, doi:10.1029/JA088iA12p10011.

McFadden, J. P., C. W. Carlson, D. Larson, M. Ludlam, R. Abiad, B. Elliott, P. Turin, M. Marckwordt, and V. Angelopoulos (2008), The THEMIS ESA Plasma Instrument and In-flight Calibration, *Space Science Reviews*, *141*, 277–302, doi:10.1007/s11214-008-9440-2.

McPherron, R. L., T.-S. Hsu, J. Kissinger, X. Chu, and V. Angelopoulos (2011), Characteristics of plasma flows at the inner edge of the plasma sheet, *Journal of*

*Geophysical Research (Space Physics)*, 116, A00I33, doi:10.1029/2010JA015923.

Meredith, N. P., R. B. Horne, S. A. Glauert, and R. R. Anderson (2007), Slot region electron loss timescales due to plasmaspheric hiss and lightning-generated whistlers, *Journal of Geophysical Research (Space Physics)*, 112, A08214, doi: 10.1029/2007JA012413.

Miyashita, Y., S. Machida, M. Nosé, K. Liou, Y. Saito, and W. R. Paterson (2012), A statistical study of energy release and transport midway between the magnetic reconnection and initial dipolarization regions in the near-Earth magnetotail associated with substorm expansion onsets, *Journal of Geophysical Research (Space Physics)*, 117, A11214, doi:10.1029/2012JA017925.

Mozer, F. S., S. D. Bale, J. W. Bonnell, C. C. Chaston, I. Roth, and J. Wygant (2013), Megavolt Parallel Potentials Arising from Double-Layer Streams in the Earth's Outer Radiation Belt, *Physical Review Letters*, 111(23), 235002, doi: 10.1103/PhysRevLett.111.235002.

Mozer, F. S., O. Agapitov, V. Krasnoselskikh, S. Lejosne, G. D. Reeves, and I. Roth (2014), Direct Observation of Radiation-Belt Electron Acceleration from Electron-Volt Energies to Megavolts by Nonlinear Whistlers, *Physical Review Letters*, 113(3), 035001, doi:10.1103/PhysRevLett.113.035001.

Nosé, M., H. Koshiishi, H. Matsumoto, P. C:son Brandt, K. Keika, K. Koga, T. Goka, and T. Obara (2010), Magnetic field dipolarization in the deep inner magnetosphere and its role in development of O<sup>+</sup>-rich ring current, *Journal of Geophysical Research (Space Physics)*, 115, A00J03, doi:10.1029/2010JA015321.

Pedersen, A., et al. (2008), Electron density estimations derived from spacecraft potential

measurements on Cluster in tenuous plasma regions, *Journal of Geophysical Research (Space Physics)*, *113*, A07S33, doi:10.1029/2007JA012636.

Reeves, G. D., M. G. Henderson, P. S. McLachlan, R. D. Belian, R. H. W. Friedel, and A. Korth (1996), Radial propagation of substorm injections, in *International Conference on Substorms, ESA Special Publication*, vol. 389, edited by E. J. Rolfe and B. Kaldeich, p. 579.

Smith, A. J., M. P. Freeman, and G. D. Reeves (1996), Postmidnight VLF chorus events, a substorm signature observed at the ground near L=4, *J. Geophys. Res.*, *101*, 24,641–24,654, doi:10.1029/96JA02236.

Stawarz, J. E., R. E. Ergun, and K. A. Goodrich (2014), Generation of High-Frequency Electric Field Activity by Turbulence in the Earth's Magnetotail, *Journal of Geophysical Research (Space Physics)*.

Suszcynsky, D. M., J. T. Gosling, and M. F. Thomsen (1993), Ion temperature profiles in the horns of the plasma sheet, *J. Geophys. Res.*, *98*, 257–262, doi:10.1029/92JA01733.

Tang, C. L., Z. Y. Li, V. Angelopoulos, S. B. Mende, K. H. Glassmeier, E. Donovan, C. T. Russell, and L. Lu (2009), THEMIS observations of the near-Earth plasma sheet during a substorm, *Journal of Geophysical Research (Space Physics)*, *114*, A09211, doi:10.1029/2008JA013729.

Whipple, E. C. (1981), Potentials of surfaces in space, *Reports on Progress in Physics*, *44*, 1197–1250.

Wygant, J. R., et al. (2002), Evidence for kinetic Alfvén waves and parallel electron energization at 4-6  $R_E$  altitudes in the plasma sheet boundary layer, *Journal of Geophysical Research (Space Physics)*, *107*, 1201, doi:10.1029/2001JA900113.

592 Wygant, J. R., et al. (2013), The Electric Field and Waves Instruments on the Radiation  
593 Belt Storm Probes Mission, *Space Science Reviews*, 179, 183–220, doi:10.1007/s11214-  
594 013-0013-7.

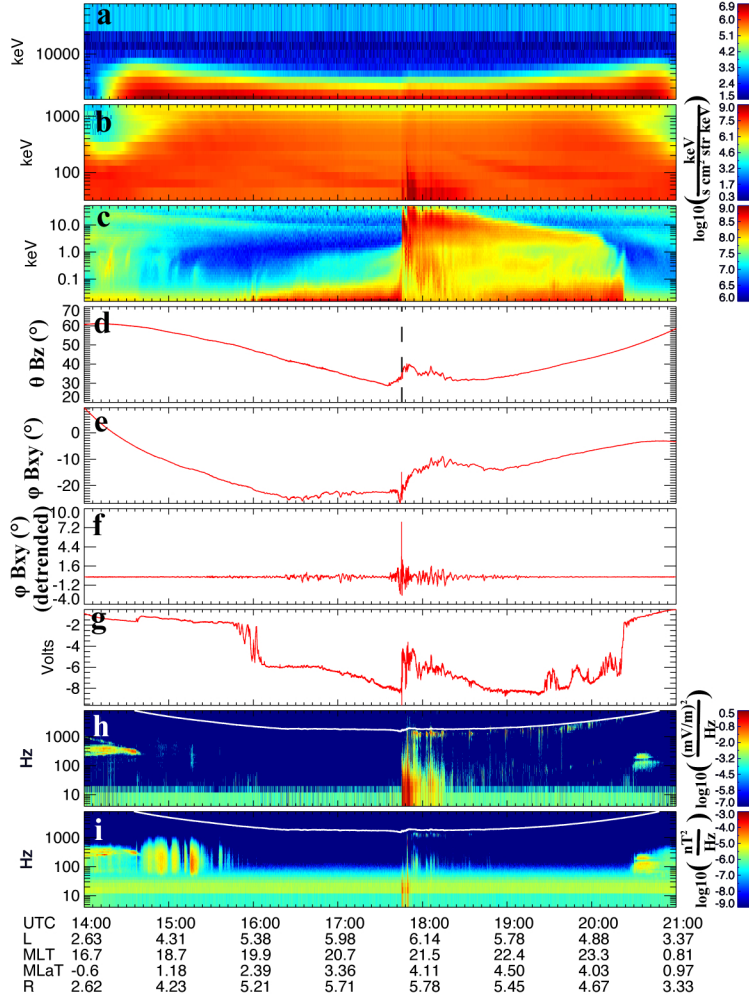


**Figure 1.** A plasma boundary observed by Van Allen Probe B on 23 June 2013, interpreted as a crossing of a dispersionless injection front. (a,b,c) Electron energy flux as a function of electron energy and time from the REPT, MagEIS, and HOPE instruments, respectively. (d) Angle of the ambient magnetic field with respect to the GSM X-Y plane. (e) Angle of the ambient magnetic field with respect to the GSM X-Z plane. (f) Same data as (e), but de-trended using a 3-minute running average. (g) Negative of the spacecraft potential. (h) Spectrogram of the wave electric field. (i) Spectrogram of the

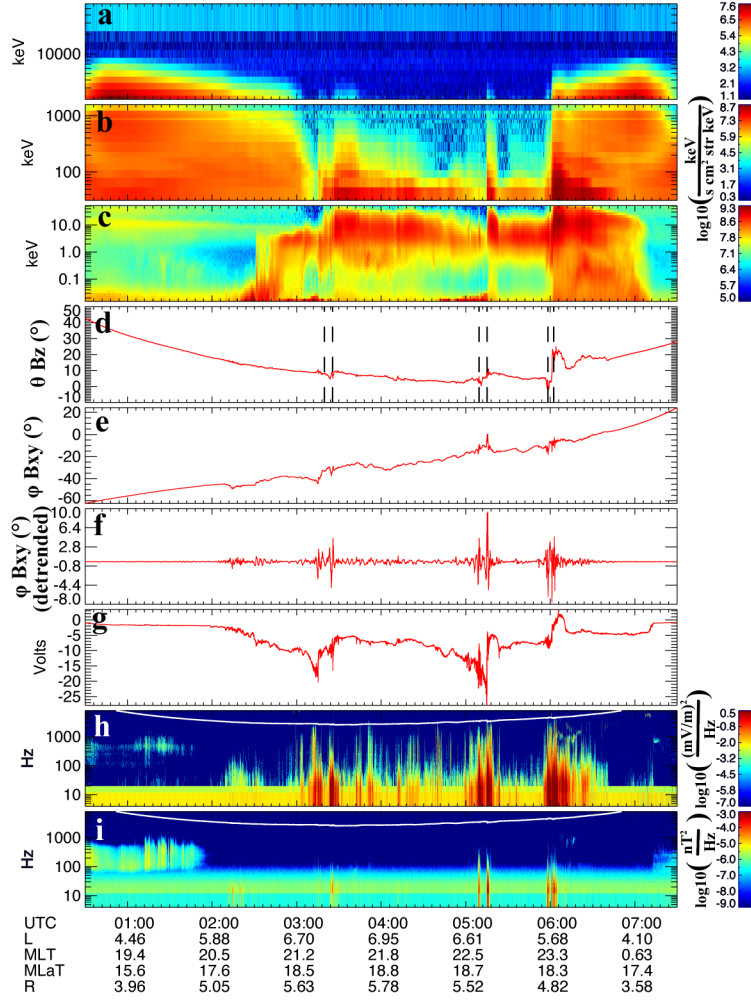


**Figure 2.** Plasma boundaries observed by Van Allen Probe A on 10 June 2013, interpreted as crossings in and out of the plasma sheet. Panels (a) through (i) have the same format as Figure 1.

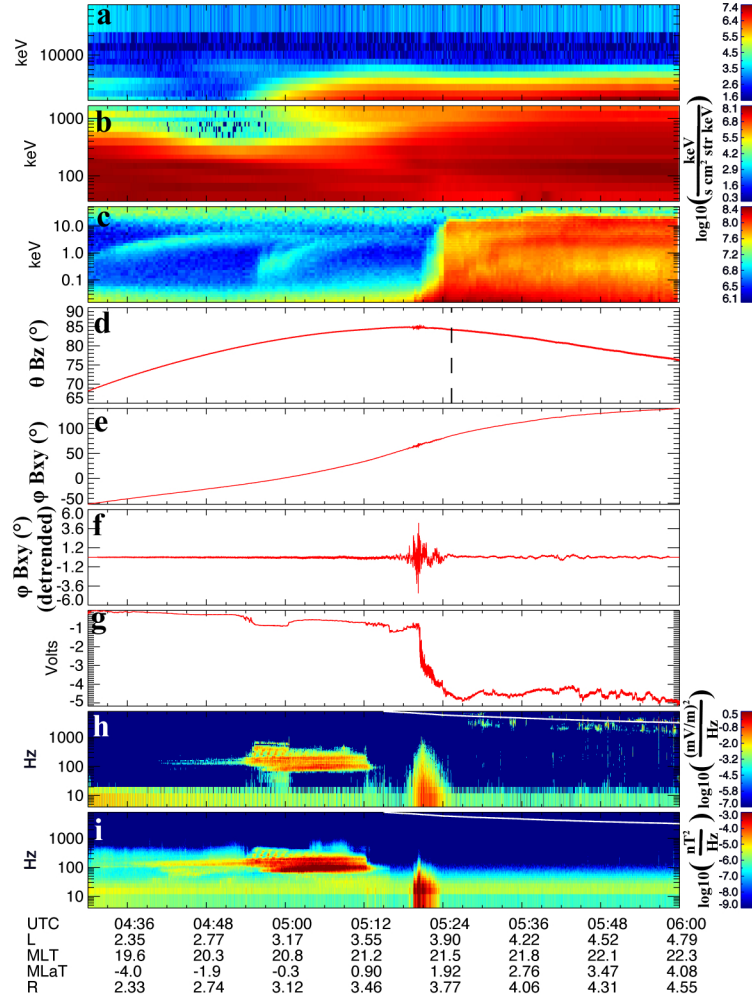


**Figure 3.** A plasma boundary observed by Van Allen Probe B on 30 March 2013, interpreted as a crossing of the plasmopause. Panels (a) through (i) have the same format as Figure 1.

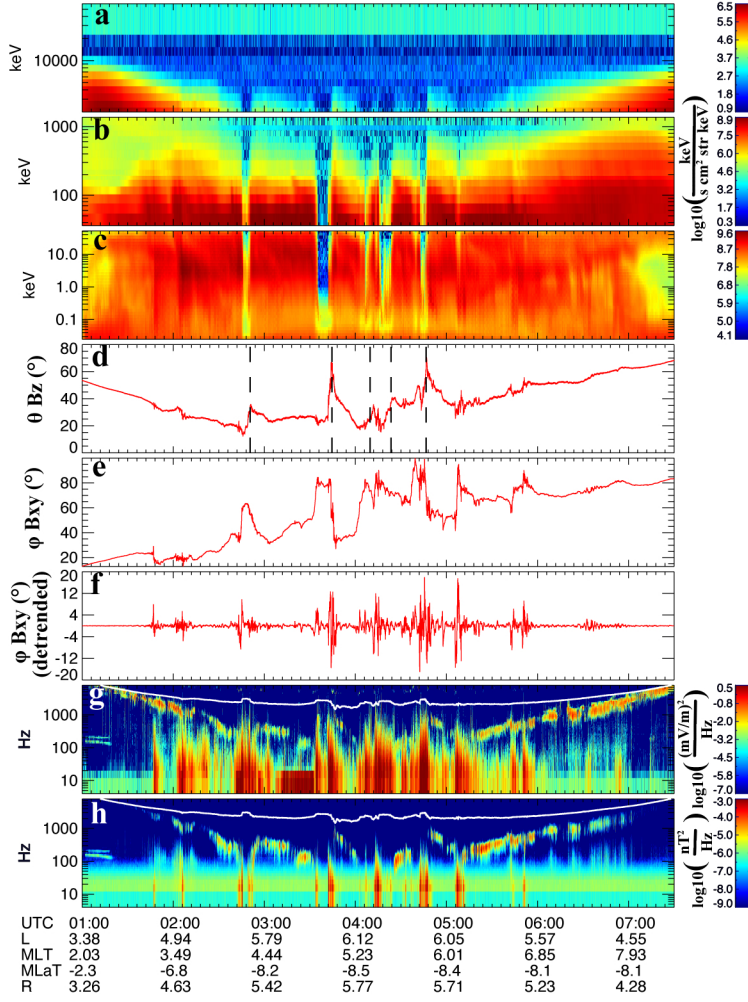


**Figure 4.** Plasma boundaries observed by Van Allen Probe B on 11 November 2012, interpreted as a crossing into and out of the lobe. Panels (a) through (f) have the same format as Figure 1. (g) Spectrogram of the wave electric field. (h) Spectrogram of the wave magnetic field.

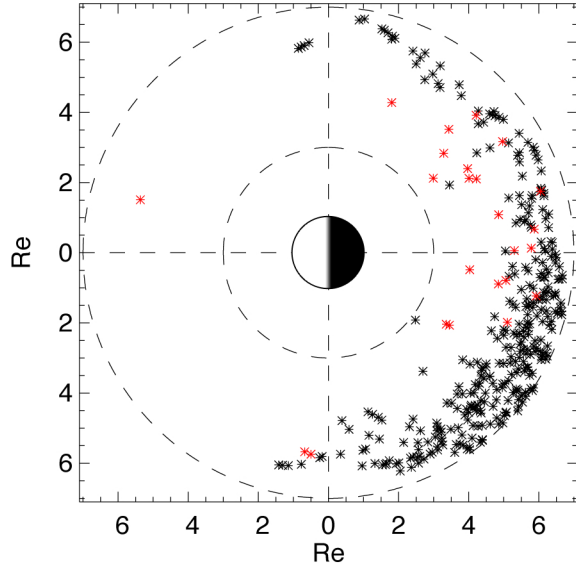


**Figure 5.** Distribution in magnetic local time and L-shell of plasma boundaries identified using a 3-minute search window (see text for details). Red symbols indicate plasmopause crossings. Circular dashed lines indicate  $L = 3$  and  $L = 7$ .

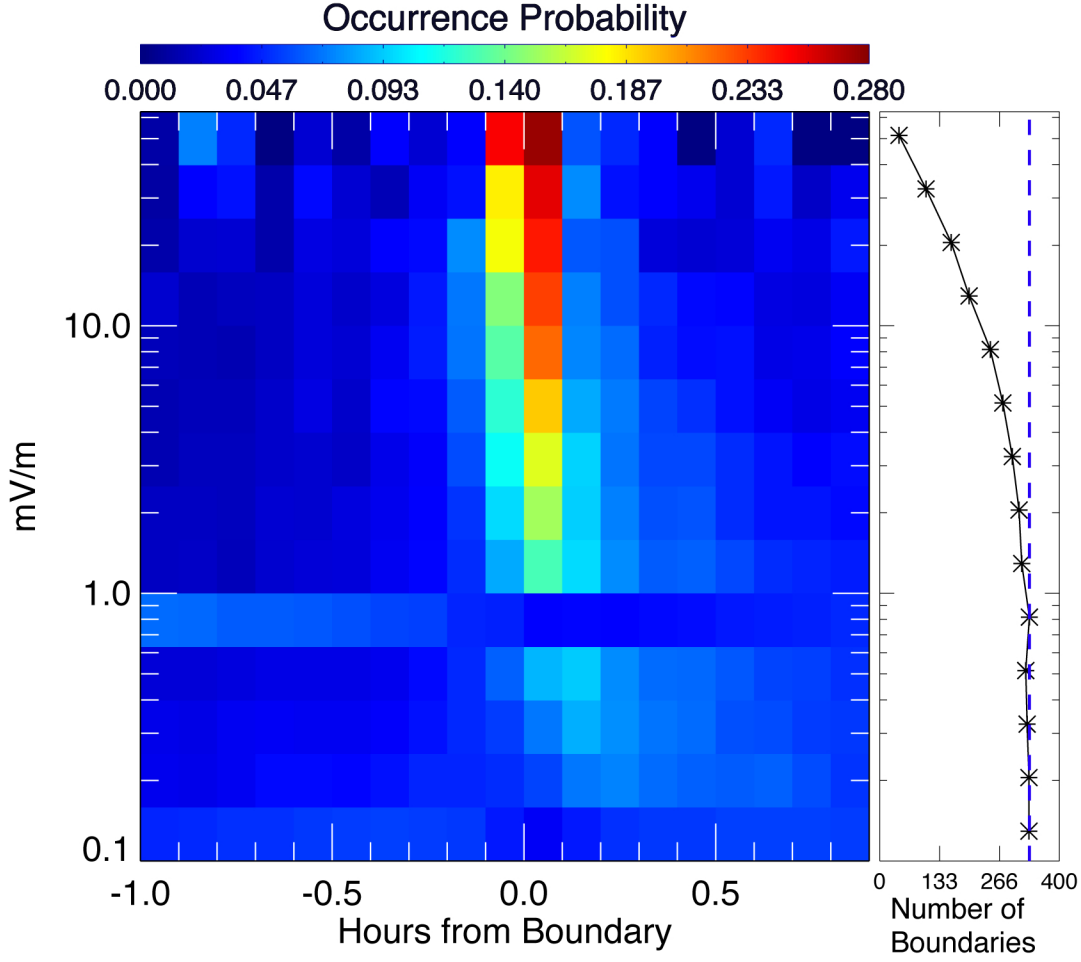


**Figure 6.** (a) Probability of observing broadband wave activity as a function of broadband wave amplitude and time away from a plasma boundary crossing. Probability distributions have been normalized to 1 in each amplitude range. (b) Number of boundary crossings with broadband wave activity in each amplitude range within  $\pm 1$  hour.

**Table 1.** Percent of identified plasma boundaries with broadband waves  $\geq 2$  mV/m within the indicated time ranges, for three different boundary-identification window definitions.

Window Size	# Boundaries	$\pm 60$ min.	$\pm 30$ min.	$\pm 10$ min.	$\pm 2$ min.
2 m	291	95.1%	91.4%	86.3%	78.3%
3 m	333	92.2%	88.3%	82.6%	73.0%
4 m	399	86.5%	83.0%	76.0%	66.0%

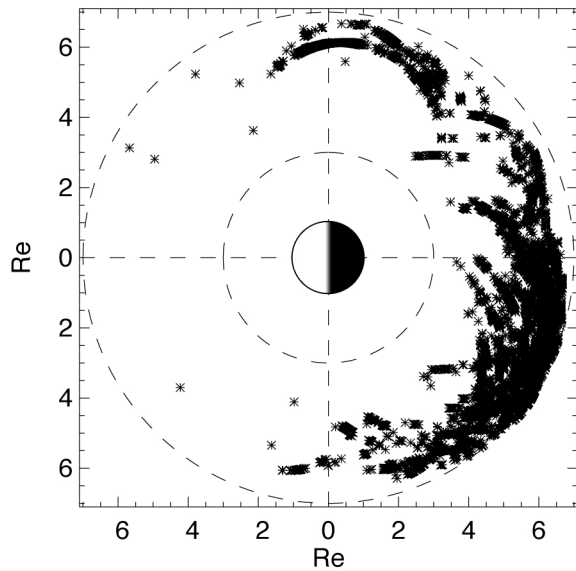


**Figure 7.** Distribution in magnetic local time and L-shell of instances of broadband wave activity  $\geq 2$  mV/m identified using a 3-minute search window (see text for details). Circular dashed lines indicate  $L = 3$  and  $L = 7$ .

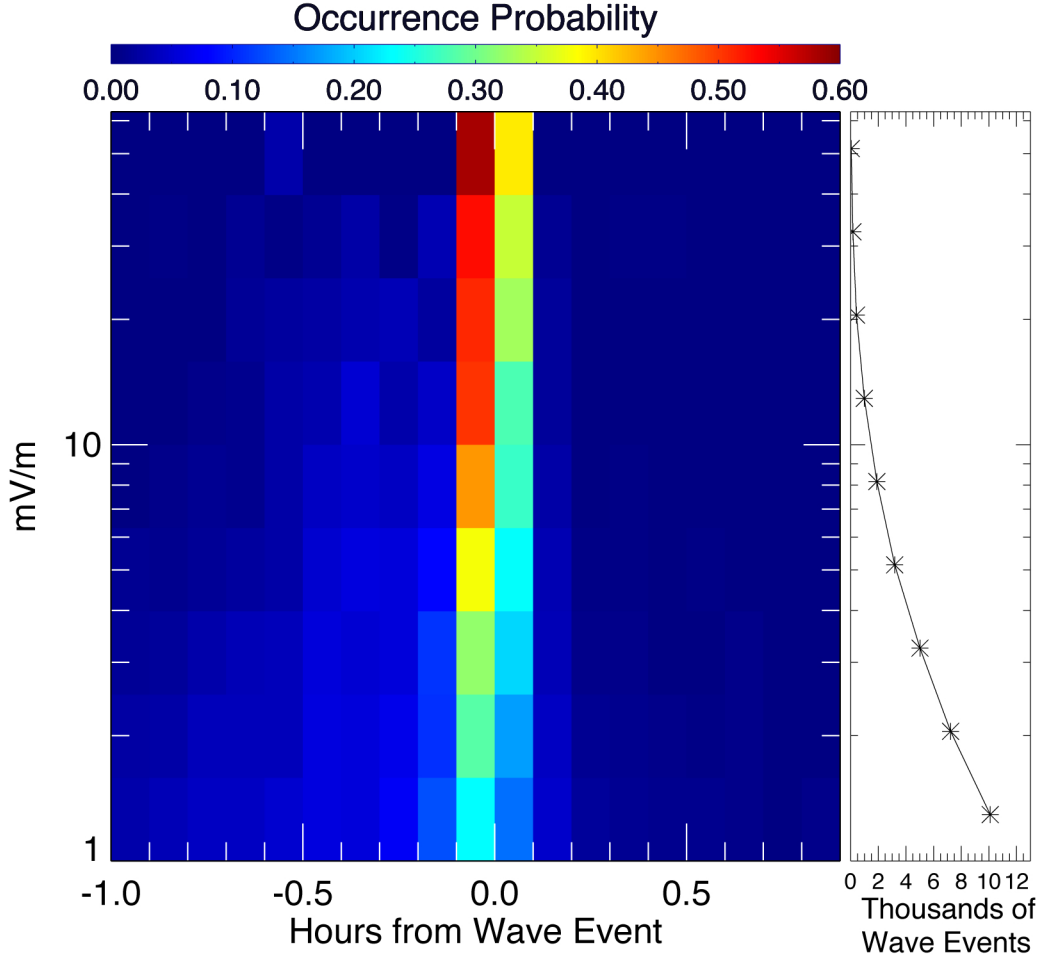


**Figure 8.** (a) Probability of observing a plasma boundary as a function of broadband wave amplitude and time away from an instance of broadband wave activity ( $\geq 2$  mV/m). Probability distributions have been normalized to 1 in each amplitude range. (b) Number of broadband wave activity instances with a plasma boundary within  $\pm 1$  hour, in each amplitude range.

**Table 2.** Percent of identified instances of broadband wave activity  $\geq 2$  mV/m with plasma boundaries within the indicated time ranges, for three different boundary-identification window definitions.

Window Size	$\pm 60$ min.	$\pm 30$ min.	$\pm 10$ min.	$\pm 2$ min.
2 m	90.0%	78.0%	61.0%	31.2%
3 m	91.0%	79.5%	61.4%	31.2%
4 m	92.0%	83.0%	65.0%	32.4%

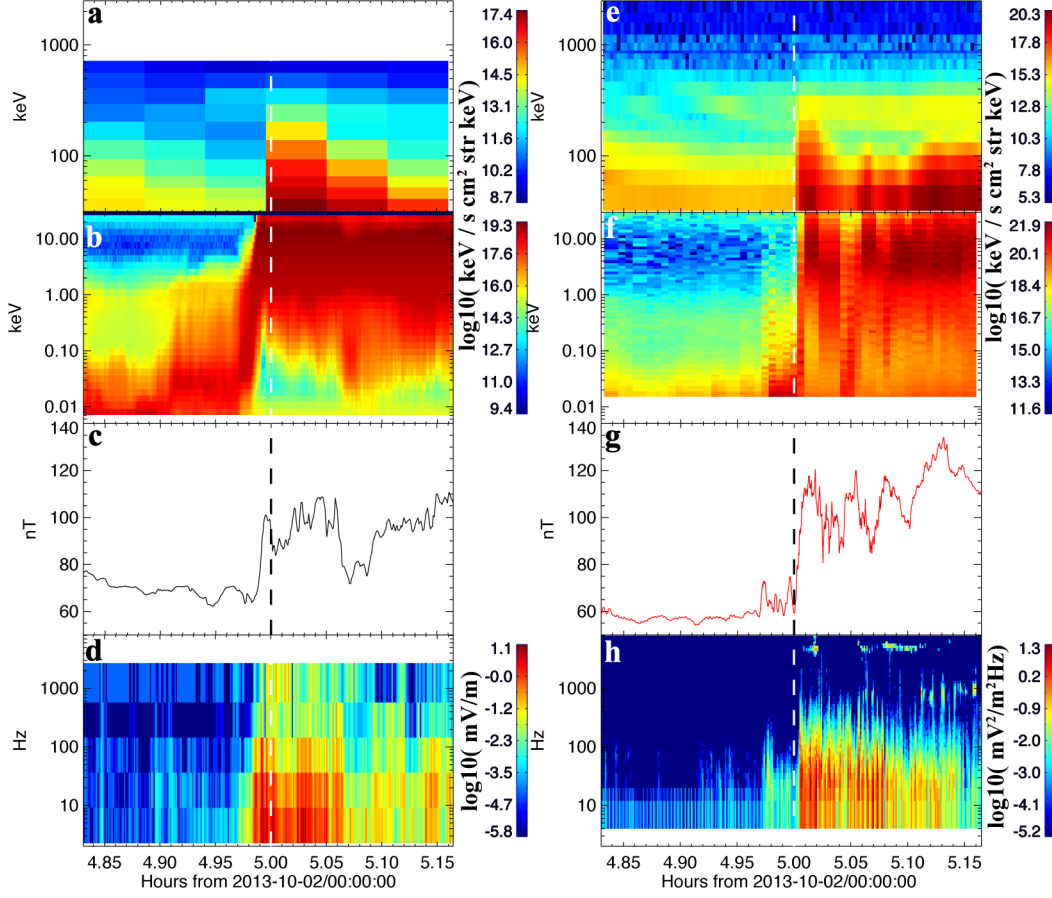


**Figure 9.** A plasma boundary crossing interpreted as a dispersionless injection front, observed by both THEMIS-D (a-d) and Van Allen Probe B (e-h) on 02 October, 2013. (a, b) Electron energy flux as a function of electron energy and time for the ESA and SST instruments, respectively. (c)  $B_z$  GSM. (d) Electric field wave amplitude in a series of bandpass bins. (e,f) Electron energy flux as a function of electron energy and time for the MagEIS and HOPE instruments, respectively. (g)  $B_z$  GSM. (h) Power spectra of the wave electric field. Vertical dashed lines appear in all plots at 05:00 UTC to illustrate that THEMIS-D encountered the plasma boundary prior to Van Allen Probe B.

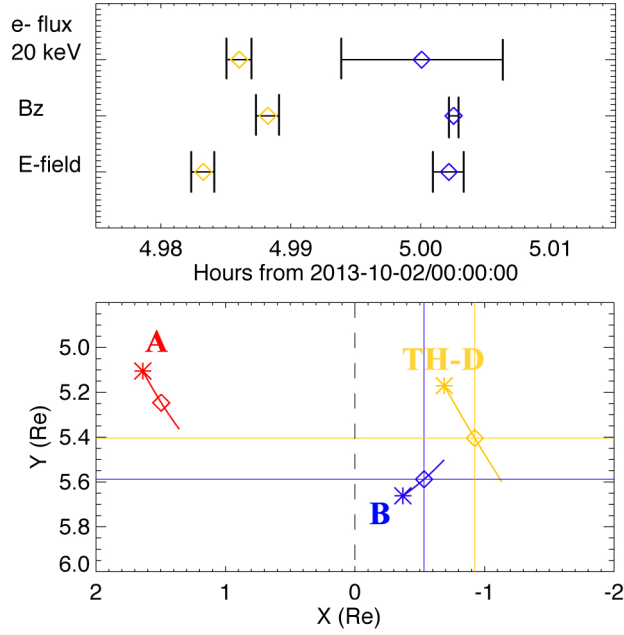


**Figure 10.** (Top) Time of boundary crossing as determined by three different indicators. Orange symbols indicate THEMIS-D, blue symbols indicate Van Allen Probe B. Error bars represent  $\pm 1$  sample uncertainties in boundary crossing time for each indicator. (Bottom) Positions of Van Allen Probe A (red), Van Allen Probe B (blue) and THEMIS-D (orange) during the time span of Figure 9. Asterisks indicate each spacecraft's position at the start of the interval. Diamonds indicate the position of each spacecraft when Van Allen Probe B encountered the plasma boundary.

**Table 3.** Propagation Delay.

Front Indicator	Time Delay (s)	X GSM Separation (km)	Velocity (km/s)
Magnetic Field	$51.5 \pm 3.2$	$2371.5 \pm 7.7$	$46.1 \pm 2.8$
Electron Flux	$50.51 \pm 22.2$	$2367.5 \pm 39.8$	$46.9 \pm 20.6$
Electric Fields	$68.0 \pm 5.0$	$2329.2 \pm 10.3$	$34.2 \pm 2.5$

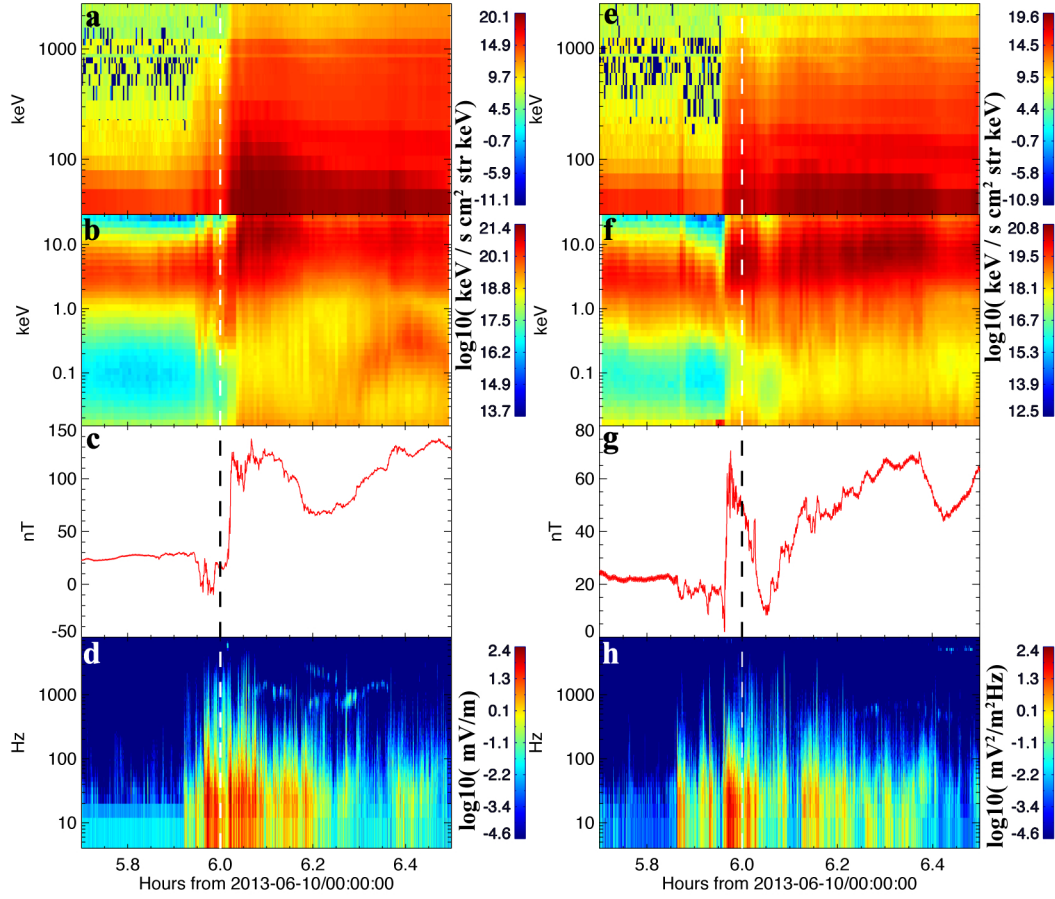


**Figure 11.** A plasma boundary crossing observed by both Van Allen Probe A (a-d) and B (e-h) on 10 June 2013. (a, e) Electron energy flux as a function of electron energy and time from the MagEIS instruments on each spacecraft. (b,f) Electron energy flux as a function of electron energy and time from the HOPE instruments on each spacecraft. (c,g)  $B_z$  GSM. (d,h) Power spectra of the wave electric field. Vertical dashed lines appear in all plots at 06:00 UTC to illustrate that Van Allen Probe B encountered the plasma boundary prior to Van Allen Probe A.

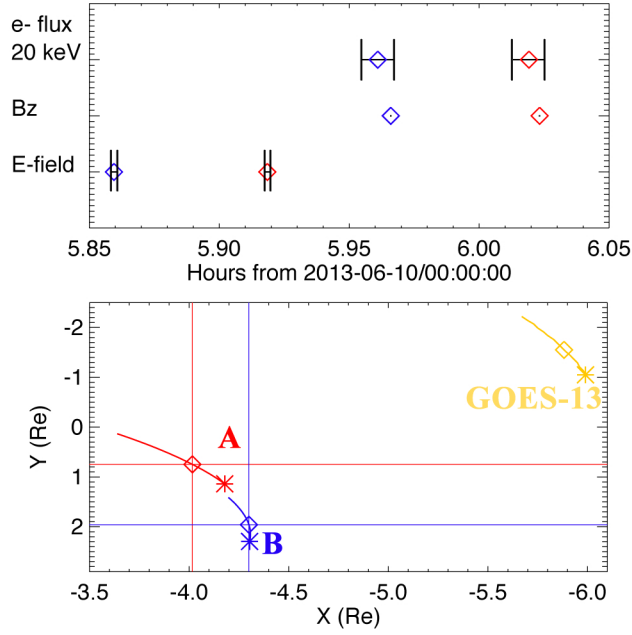


**Figure 12.** (Top) Time of boundary crossing as determined by three different indicators. Red symbols indicate Van Allen Probe A, blue symbols indicate Van Allen Probe B. Error bars represent  $\pm 1$  sample uncertainties in boundary crossing time for each indicator. Error bars on Bz are too close together to be visible on this scale. (Bottom) Positions of Van Allen Probe A (red), Van Allen Probe B (blue) and GOES-13 (orange) during the time span of Figure 11. Asterisks indicate each spacecraft's position at the start of the interval. Diamonds indicate the position of each spacecraft when Van Allen Probe B encountered the plasma boundary.